Local structure in crystalline, glass and melt states of a hybrid metal halide perovskite

Akash Singh,[1,2] Damara Dayton,[3] Dylan M. Ladd,[3] Guy Reuveni,[4] Piotr Paluch,[5,6] Lionel Montagne,[6] Julian Mars,[3] Omer Yaffe,[4] Michael Toney,[3,7,8] G. N. Manjunatha Reddy,[6] David B. Mitzi [1,9*]*

[1]Department of Mechanical Engineering and Materials Science, Duke University, Durham, North Carolina 27708, USA

[2]University Program in Materials Science and Engineering, Duke University, Durham, North Carolina 27708, USA

[3]Materials Science and Engineering Program, University of Colorado Boulder, Boulder, CO 80303, USA

[4]Department of Chemical and Biological Physics, Weizmann Institute of Science, Rehovot 7610001, Israel

[5]Centre of Molecular and Macromolecular Studies, Polish Academy of Sciences, Sienkiewicza 112 St., Lodz 90-363, Poland

[6] University of Lille, CNRS, Centrale Lille Institut, Université d' Artois, UMR 8181, Unité de Catalyse et Chimie du Solide, Lille F-59000, France

[7]Renewable and Sustainable Energy Institute, University of Colorado Boulder, Boulder, CO 80309, USA

[8]Department of Chemical and Biological Engineering, University of Colorado Boulder, Boulder, CO 80309, USA

[9]Department of Chemistry, Duke University, Durham, North Carolina 27708, USA

*Corresponding author: david.mitzi@duke.edu, gnm.reddy@univ-lille.fr

Abstract:

The pursuit of structure-property relationships in crystalline metal halide perovskites (MHPs) has yielded an unprecedented combination of advantageous characteristics for wide-ranging optoelectronic applications. While crystalline MHP structures are readily accessible through diffraction-based structure refinements, providing a clear view of associated long-range ordering, the local structures in more recently discovered glassy MHP states remain unexplored. Herein, we utilize a combination of Raman spectroscopy, solid-state nuclear magnetic resonance (NMR), Fourier transform infrared spectroscopy, in-situ X-ray diffraction (XRD) and pair distribution function (PDF) analysis to investigate the coordination environment in crystalline, glass and melt states of the 2D MHP [(S)-(−)-1-(1-naphthyl)ethylammonium]$_2$PbBr$_4$. While crystalline SNPB shows polarization-dependent Raman spectra, the glassy and melt states exhibit broad features and lack polarization dependence. Solid-state NMR reveals disordering at the organic-inorganic interface of the glass due to significant spatial disruption in the tethering ammonium groups and the corresponding dihedral bond angles connecting the naphthyl and ammonium groups, while still preserving substantial naphthyl group registry and remnants of the layering from the crystalline state (deduced from XRD analysis). Moreover, PDF analysis demonstrates the persistence of corner-sharing octahedra in the inorganic Pb-Br framework of the melt/glass phases, but with a loss of structural coherence over length scales exceeding 8-10 Å due to disorder in the inter- and intra-octahedra bond angles/lengths. These findings deepen our understanding of diverse MHP structural motifs and how structural alterations within the MHP glass affect properties, offering potential for advancing next-generation phase change materials and devices.

Introduction

Hybrid metal halide perovskites (MHPs) are a class of semiconducting materials that have garnered interest in the field of optoelectronics, driving remarkable advancements in photovoltaic,[1, 2] emitter,[3] sensing,[4-6] and photonic devices.[7] A key and distinguishing attribute of MHP semiconductors is the ability to combine organic and inorganic components, allowing for multifunctional and synergistic effects that arise from the interaction between these two chemical domains.[8-12] Recent upsurge in the versatile synthesis of MHPs and the associated device applications[13] have been greatly facilitated by advancements in understanding of structure-property relationships.[8-10] For example, effective MHP dimensionality can be tuned from three-dimensional (3D) to two- (2D) or even one- (1D) dimensional, as determined by the topology of the long-range connectivity of the inorganic framework through the corner sharing of metal halide octahedra.[14-18] The presence of certain organic cations can also introduce configurational strain, leading to alternative inorganic connectivity patterns, resulting in the formation of edge-shared or face-shared octahedra, or a combination thereof.[11, 19, 20] Additionally, distortions in the octahedra associated with the inorganic framework impact many interesting MHP properties, including bandgap,[21, 22] broadband light emission,[23, 24] strong optical non-linearity,[25] Rashba splitting,[26-28] and ferroelectricity[29]. Through meticulous structural engineering and a comprehensive understanding of the interactions between the organic and inorganic sublattices, the properties of MHPs can be finely tuned, resulting in enhanced performance for diverse applications.[23, 25, 29-36]

Notably, structure-property relationships in hybrid MHPs have been pursued and advanced by focusing on *crystalline hybrids*, given facile access to well-defined structure refinements that can provide a clear view of the time-averaged long-range ordering. In contrast to the study of well-ordered hybrid MHPs, insights into disorder within equilibrium or non-equilibrium structures, such as for organic/inorganic interfaces[37] and grain boundaries,[38, 39] various dimensionality defects,[37] and dynamical disorder,[40-42] remain more challenging to obtain. In this context, the [(*S*)-(−)-1-(1-naphthyl)ethylammonium]$_2$PbBr$_4$ (SNPB) system is highly intriguing, as it not only exhibits unique properties in the crystalline state, including chirality transfer and significant inorganic octahedra distortion,[30] but also offers access to both molten and glassy states and a first opportunity to investigate their local structure and resulting properties.[43, 44] The discovery of a glassy state in MHPs opens up new avenues for studying the characteristics of *globally structurally*

disordered versions of MHP semiconductors and for exploring the diverse range of properties that can arise from variations in the local structure of the glass compared to its crystalline counterpart.

Recent examples of structure-property studies have already sparked interest in various other glassy hybrids, including metal-organic frameworks (MOFs)[45] and non-halide-based organometallic perovskites.[46, 47] These studies have demonstrated how altering the local coordination influences the porosity,[48-50] optical,[51] electronic, and thermal properties[52] of these hybrid materials, with profound implications across a wide range of applications, including gas storage, chemical separation, carbon capture, controlled drug release, ion conduction as well as in the development of memory and thermoelectric devices.[46, 51, 53] A detailed thermal analysis study using differential scanning calorimetry (DSC) for SNPB has provided insights into glass transition, cold crystallization, and melting temperatures, as well as underlying crystallization kinetics.[44] Glasses derived from SNPB perovskite also exhibit distinct optoelectronic properties, including a blue shift of ~50 nm (or ~0.4 ev) in optical absorption[44] and a two-orders decrease in electrical conductivity compared to the crystalline state.[54] The observed property changes in the glassy state of MHPs, which likely arise from variations in the local coordination environment, coupled with the ability to reversibly switch between crystalline and glassy state, hold great potential for expanding the application space of MHPs. However, despite the promising possibilities presented by non-crystalline MHP states, our current understanding of the structure and its connection to the observed properties in both the molten and glassy states is still limited, highlighting the need for further investigation.

To gain insights into the local coordination environment in non-crystalline states of MHPs, the present study comprehensively compares crystalline, glass, and molten states by combining temperature-dependent Raman spectroscopy,[55, 56] solid-state nuclear magnetic resonance (ss-NMR),[37, 57] Fourier transform infrared (FTIR) spectroscopy, in-situ temperature dependent X-ray diffraction (XRD), and X-ray total scattering for pair distribution function (PDF) analysis.[46, 58] The polarization-dependent Raman spectra of crystalline SNPB show well-defined narrow features corresponding to the long-range order, but the glassy state lacks this polarization dependence and shows broader features, due to the absence of such ordering. The ss-NMR results point to the glassy state preserving ordering among the naphthyl groups, thereby supporting/maintaining a nominally layered structure, consistent with the observations from the X-ray diffraction

experiments[44, 59] (which show a broad low-angle peak, consistent with loosely correlated layering among the lead(II) bromide component in both the melt/glass states and suggesting a weak smectic-like[60] or turbostratic-like[61, 62] ordering within these states). However, notable displacements appear among the tethering ammonium groups and the dihedrals connecting the naphthyl and ammonium groups, resulting in a loss of ordering within this region of the structure. FTIR spectroscopy further highlights a weakening of the hydrogen-bonding interactions at the organic-inorganic interface in the glass. The disordering of the tethering group subsequently affects the local octahedra tilting within the metal halide framework, while still maintaining the short-range coordination around the Pb cation. We conclude from PDF analysis that corner-sharing connectivity remains dominant in the amorphous states. Structural order in the Pb-Br layers, however, does not exceed lengths of ~10 Å in the glass or melt, suggesting that deformation of nominally intact inorganic layers disrupts the long-range ordering observed in the crystal phase. The disruption in the inorganic framework (e.g., Pb-Br-Pb bond angles and framework connectivity) provides a likely explanation for the previously reported drastic decrease in observed electrical conductivity and blue-shift of the absorption onset for the glass.[44,54] The current study reveals insights into the structure and the intricate interplay between structure and properties in the realm of molten and glassy MHPs, paving the way for transformative advancements among these disordered semiconductors.

Results and Discussion

To provide an initial comparison of the structural characteristics of SNPB crystalline and glassy states, room temperature (300 K) polarization-orientation (PO) Raman scattering measurements were conducted (see Figure S1 for details of setup). The variation in Raman-scattering intensity was measured as a function of the angle between the linear polarization of the excitation laser and an arbitrary axis in the plane of the crystal surface, which reflects the average symmetry of the measured sample.[55] Figures 1(a) and (b) display Raman intensity heatmaps of the crystalline and glass states (see Experimental Section), respectively. The crystalline PO map exhibits clear polarization dependence, as expected for an ordered crystal, whereas the analogous glassy state map shows no polarization dependence, typical for glassy materials lacking long-range order. To preclude the effects of dynamic disorder arising from thermal vibrational effects, the Raman spectra of the two states were measured at cryogenic temperature (T = 10 K; see Figure S2 for full

sequence of temperature-dependent Raman spectra). For the crystalline state, sharp and high intensity peaks reflect the distinct and well-defined Raman active modes (Figure 1c). The glassy state exhibits scattering in a similar frequency range as the crystalline state, albeit with significantly broader features. The observed relationship in Raman data between the crystalline and glassy states of SNPB aligns with previous findings in materials such as crystalline and glassy quartz[63] and confirms the identification of the melt-quenched phase of SNPB as glassy. Furthermore, similar spectral features are observed between the glassy and melt states on comparing the reduced Raman spectra — obtained by dividing the raw spectrum by the temperature-dependent Bose-Einstein distribution (see Experimental Section) [64, 65] — to account for thermal effects between different states near the vicinity of melting temperature (T_m) of SNPB (Figure 1d). Notably, Raman features in the frequency range below 120 cm^{-1} can generally be assigned to $PbBr_6$ octahedra rocking/twisting modes, as well as Pb-Br bond bending, twisting and stretching modes.[66-68] While the analogous features in the glass and melt phases are too diffuse to definitively assign to specific lattice modes, the maintenance of spectral weight in the relevant frequency range suggests that the $PbBr_6$ octahedra persist into these phases, a point that will be further discussed for the solid state NMR and PDF analyses (*vide infra*).

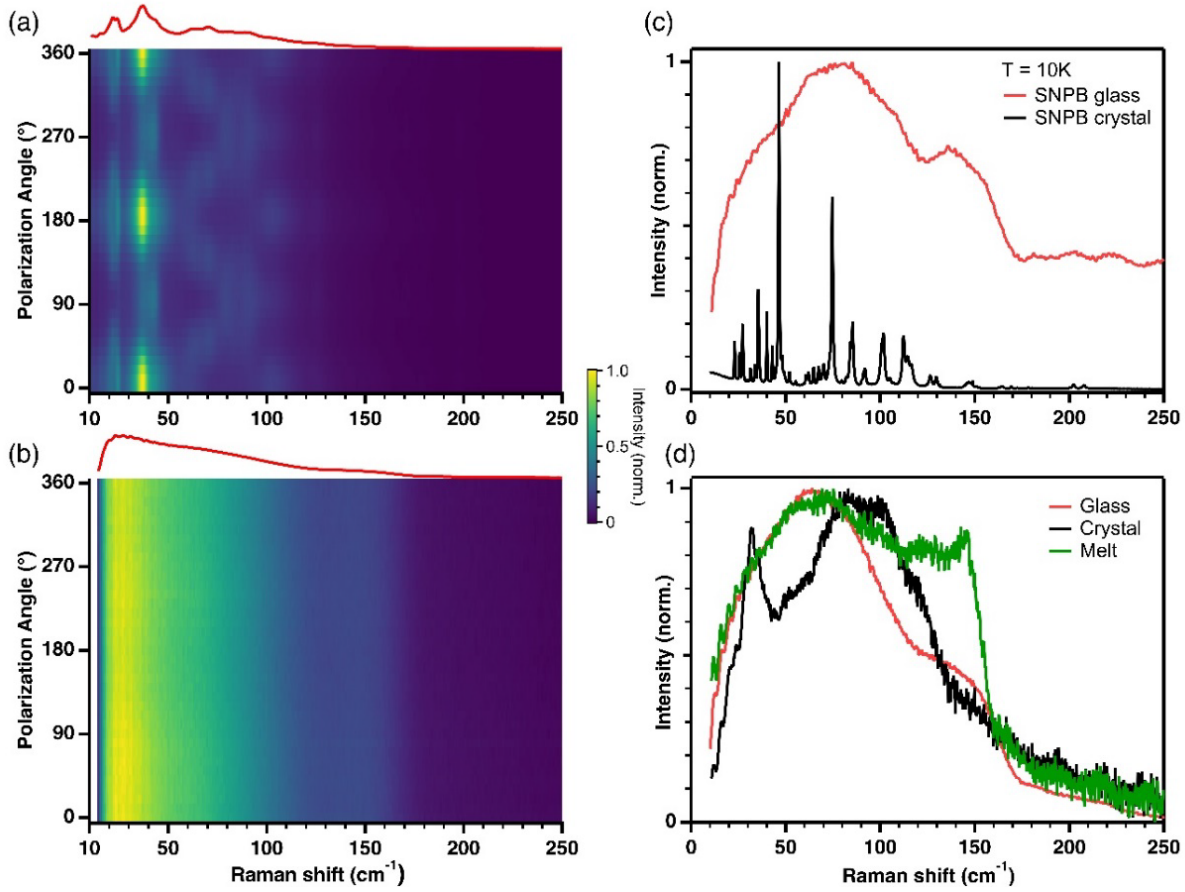

Figure 1. Polarization-orientation (PO) Raman intensity heatmaps of the crystalline (a) and glassy (b) states of SNPB at 300 K are shown, with the red curves at the tops of the panels displaying the unpolarized spectra obtained by summing over all polarization angles. The Raman spectra of the glassy and crystalline states at 10 K are compared in (c), while (d) presents the reduced Raman spectra (see Experimental Section) of the glassy, crystalline, and melt states, reduced from 345K, 446K, and 458K, respectively.

To further explore the different local chemical environments of organic cations and organic-inorganic interfaces in the crystalline and glassy states of SNPB, solid-state 1D ^{1}H, ^{13}C and ^{207}Pb Magic-Angle Spinning (MAS) NMR spectra were collected and analyzed.[37, 69-71] Specifically, ^{1}H chemical shifts are sensitive to hydrogen bonding interactions, π–π stacking, C-H-π interactions, and relative orientations of organic cations with respect to PbX_6 octahedra, whereas ^{13}C chemical

shifts reflect the molecular conformation within the perovskite (or disordered) framework. On the other hand, ^{207}Pb chemical shifts are sensitive to changes in the inorganic framework, including PbX_6 coordination, octahedral distortions, and the type of halogen in the lead halide octahedra.

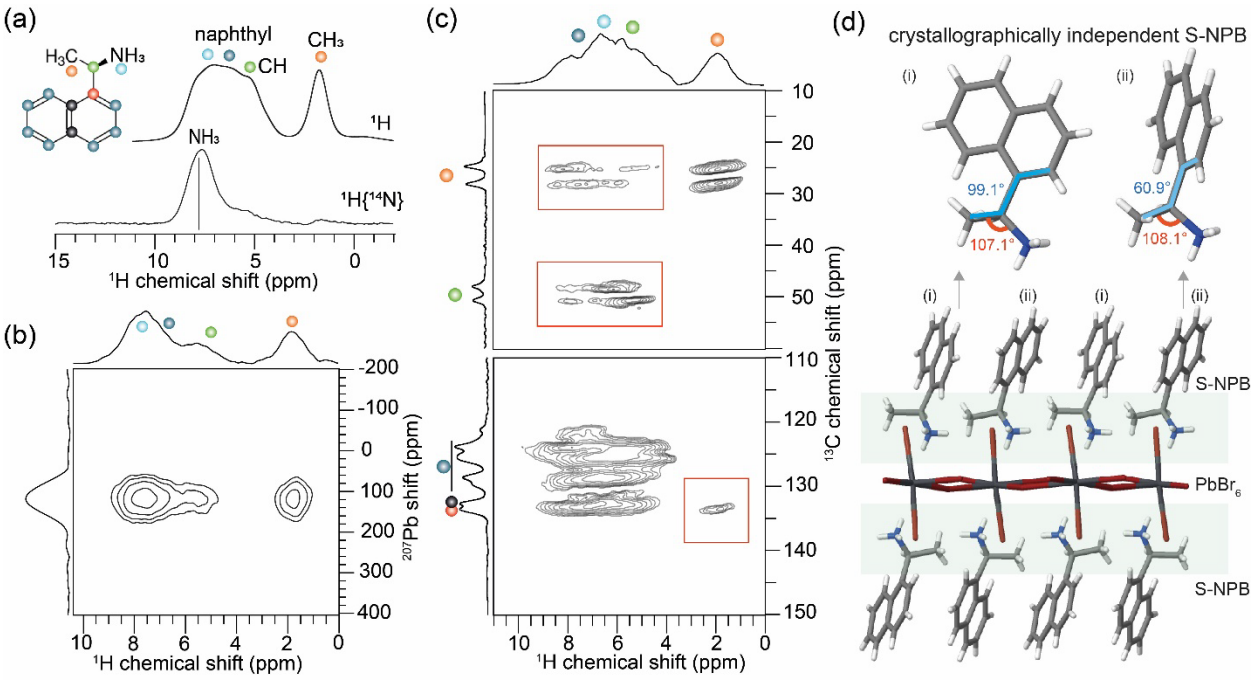

Figure 2. Local structures and packing interactions in crystalline SNPB. (a) 1D ^{1}H and ^{1}H{^{14}N} MAS NMR spectra. (b) 2D ^{1}H-^{207}Pb correlation spectrum and (c) ^{1}H-^{13}C correlation spectrum with aliphatic (top) and aromatic regions (bottom) expanded, with solid red boxes depicting through-space proximity between tethered groups in spacer cations. ^{1}H and ^{13}C peaks corresponding to the naphthyl and aliphatic sites are color coded as depicted in the inset shown in (a). (d) crystal structure of SNPB depicting two crystallographically independent spacer cations (labeled "i" and "ii") by means of different dihedral angles between the naphthyl and ammonium groups. All spectra were acquired at 18.8 T (Larmor frequencies: ^{1}H = 800.1 MHz, ^{13}C= 201.3 MHz and ^{207}Pb= 167.4 MHz) and at room temperature.

For crystalline SNPB, the obtained resolution in the ^{1}H NMR spectrum (Figure 2a) enables the identification of the CH_3 groups (1.7 ppm, orange dot); but the resolution is inadequate to distinguish between NH_3, CH and naphthyl sites that overlap to yield a broad signal in the range

of 4-9 ppm. However, ^{1}H sites in the vicinity of the ^{14}N sites can be selectively excited and detected using ^{1}H{^{14}N} filters (see bottom panel of Figure 2a)—i.e., the ^{1}H chemical shift associated with the NH_3 groups (7.8 ppm, cyan dots) is displaced to a higher ppm value compared to the NH_3 response (~6.5 ppm) of 3D methylammonium lead bromide ($MAPbBr_3$),[72] indicating stronger hydrogen bonding between (*S*)-(−)-1-(1-naphthyl)ethylammonium and the $PbBr_6$ octahedra in SNPB. Single crystal structure analysis indicates the presence of two crystallographically independent spacer cations with different hydrogen bonding interactions between the NH_3 sites and the $PbBr_6$ octahedra and distinct naphthyl side-chain conformations (Figure 2d).[30, 44] However, ^{1}H NMR does not provide sufficient resolution to resolve these distinct cations. The subtleties in the chemical shifts are within the full width at half-maximum (FWHM) of ~1110 Hz (1.38 ppm). In comparison, ^{13}C NMR provides enhanced resolution to gain insights into the different local chemical environments of carbon atoms within the organic spacer cations and the naphthyl side-chain conformations. Additionally, in cross-polarization (CP) MAS experiments, ^{13}C signals are enhanced by polarization transfer from adjacent ^{1}H sites via ^{1}H-^{13}C dipole-dipole interactions. By adjusting the CP contact time, the ^{13}C signals of directly bonded CH groups and through-space CH moieties can be identified and detected (Figure S3). Enhanced resolution in the ^{13}C CP-MAS spectrum allows naphthyl CH moieties (120-130 ppm range, blue dot, Figure S3) and quaternary carbon atoms (127-130 ppm indicated by a grey dot and 133-135 ppm depicted by a red dot) and, sidechain CH (48 and 51 ppm, green dot) and CH_3 (25 and 28 ppm, orange dot) groups to be distinguished. Both CH and CH_3 groups exhibit two sets of signals each, which reflects the two crystallographically independent molecules that differ in their dihedral angles (i.e., providing the resolution that is missing within the ^{1}H NMR spectrum). In addition, 1D ^{207}Pb NMR shows a broad distribution of signals due to large chemical shift anisotropy and spin-orbit coupling, which cannot be completely averaged by MAS experiments. For crystalline SNPB, a ^{207}Pb chemical shift centered at ~110 ppm (Figure S4) is observed due to chemically equivalent ^{207}Pb atoms, although each Pb atom is bonded to apical and in-plane Br atoms.

Further insights into the packing interactions within the organic layers as well as the organic-inorganic interfaces in crystalline S-NPB can be obtained by analyzing the 2D ^{1}H-^{207}Pb and ^{1}H-^{13}C correlation spectra. In such spectra, 2D peaks are produced for the spatially proximate and through-space dipolar-coupled ^{1}H-^{207}Pb and ^{1}H-^{13}C sites over sub-nanometer distances. The 2D ^{207}Pb-^{1}H spectrum (Figure 2b) exhibits well-resolved peaks that correlate ^{207}Pb shift (~110 ppm)

with the NH_3 (7.8 ppm), CH (5-6 ppm) and CH_3 (1.7 ppm) proton sites, confirming the sub-nanometer proximities between the organic spacer cations and the lead bromide octahedra. These results are further corroborated by the analysis of 2D ^{1}H-^{13}C spectrum (Figure 2c): two distinct 2D peaks between ^{1}H (5.9 ppm) and ^{13}C (48 ppm), and ^{1}H (5.3 ppm) and ^{13}C (51 ppm) are attributed to the distinct CH moieties with C-H…Br interactions and associated C-H…Br distances of 2.99 Å and 3.19 Å, respectively, as depicted in the solid red boxes in the top panel of Figure 2c.[30] In addition, 2D peaks correlating the ^{13}C chemical shifts at 25 ppm and 28 ppm with the ^{1}H chemical shift of 1.7 ppm corresponding to terminal CH_3 groups are resolved. In the aromatic region, 2D peaks associated with the naphthyl CH moieties (blue dots) and the through-space interactions between the quaternary carbon atoms (133-135 ppm, black and red dots) and the CH_3 groups (1.7 ppm) are observed (solid red box in bottom panel of Figure 2c). Two crystallographically independent organic spacer cations (Figure 2d) contribute to the different 2D peaks in the ^{1}H-^{13}C correlation spectrum, of which tethered CH_3 and CH carbon sites are well-resolved and distinguished, suggesting that the organic-inorganic interface in crystalline SNPB exhibits different non-covalent interactions. The interplay among these non-covalent interactions during the vitrification process may contribute to the different packing interactions in the glass, as discussed below.

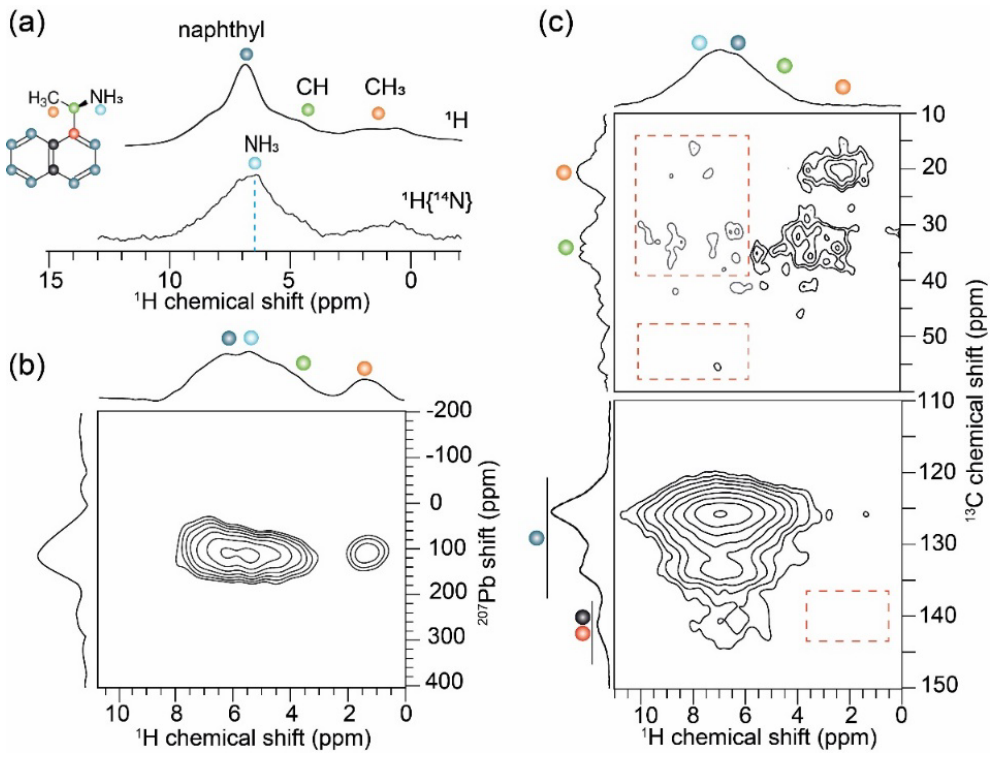

Figure 3. Local structures and packing interactions in glassy SNPB. (a) 1D ^{1}H and $^{1}H\{^{14}N\}$ MAS NMR spectra. (b) 2D ^{1}H-^{207}Pb correlation spectrum and (c) ^{1}H-^{13}C correlation spectrum with aliphatic (top) and aromatic (bottom) regions expanded, with dashed red boxes representing the disruption of peaks indicating locally disordered tethered groups in spacer cations. ^{1}H and ^{13}C peaks corresponding to the naphthyl and aliphatic sites are color coded as depicted in the inset shown in (a). All spectra were acquired at 18.8 T (Larmor frequencies: ^{1}H = 800.1, ^{13}C= 201.3 MHz and ^{207}Pb= 167.4 MHz) and at room temperature.

Next, we applied a similar measurement approach to study the glassy phase of SNPB, to gain insights into the changes in local order and packing interactions upon the crystal-to-glass transformation (see Experimental Section). Changes in the local chemical environments (sub-nanometer to nanometer distances) are expected to produce different displacements of the chemical shifts in the 1D spectra, whereas changes in through-space interactions are best observed through changes in 2D peak intensities and widths. Relatively broad features in the ^{1}H NMR spectrum of glassy SNPB (i.e., compare Figure 2a and Figure 3a) confirm the presence of local disorder as indicated by the different distributions of CH_3 (0-3 ppm) peaks and the line broadening (FWHM of ~2420 Hz or ~3.03 ppm) associated with the CH sites (4-6 ppm). The changes associated with

disordering are also reflected in the ^{14}N-filtered ^{1}H MAS spectrum, whereby the peak broadening associated with NH_3 groups is detected in the 5-9 ppm range with FWHM of over 2300 Hz (or ~2.87 ppm) due to the different distributions of ^{1}H chemical shifts (as opposed to relatively narrow peak at 7.8 ppm with FWHM of ~1100 Hz, or 1.34 ppm, in crystalline SNPB) due to the weaker hydrogen bonding interactions with the lead bromide octahedra. These results are corroborated by analyzing 2D ^{1}H-^{14}N and ^{1}H-^{1}H correlation spectra (Supporting Information and Figure S5), which show different 2D peak intensities and frequencies, arising from the changes in packing interactions including hydrogen bonding interactions in the vicinity of tethered groups (NH_3 moieties) of organic spacer cations and $PbBr_6$ slabs. The 2D ^{1}H-^{14}N peaks originating from inter and intramolecular dipole-dipole interactions are detected in the SNPB crystalline sample (Figure S5a, solid red box), whereas such peaks are poorly detected (or even undetected) in the SNPB glass (Figure S5b, dashed red box). The 2D ^{1}H-^{207}Pb correlation spectrum exhibits similar trends (Figure 3b). However, a broad ^{207}Pb feature of the glassy SNPB phase appears at ~100 ppm with FWHM of ~75 kHz (448 ppm), hinting at unresolvable local structural changes within the inorganic lead bromide octahedron itself upon vitrification (Figure S4).[73] The most notable point is that the local disorder at the organic-inorganic interface, as mediated by disordering of the tethering groups attached to the naphthyl rings, particularly contributes to the glassy phase, as observed by the changes in the position and FWHM of the chemical shift of CH_3, CH, and NH_3 sites. The relatively insignificant change in the ^{207}Pb shifts (~10 ppm) suggests that the octahedral connectivity is less perturbed across the glass-crystalline transition, though the peak broadening (FWMH ~75 kHz or 448 ppm) indicates changes in local $PbBr_6$ octahedral tilting and distortions, as further supported by PDF anlysis presented below. If structural collapse of corner-sharing $PbBr_6$ octahedra were to occur, then the displacement in the ^{207}Pb shift would be expected to be of the order of a few 100 ppm towards a lower frequency.[74] However, the analysis cannot exclude the possibility of existence of a small concentration of undercoordinated Pb atoms or the presence of edge/face-shared $PbBr_6$ octahedra, below the sensitivity and resolution limit for the analysis of ^{207}Pb shifts—e.g., due to possible disruption in the connectivity among what remains of the 2D $PbBr_4^{2-}$ sheets within the glass phase.

Locally disordered sites at the interface were further confirmed by analyzing 2D peaks in the ^{1}H-^{13}C spectrum. Weak intensity (or the absence of) 2D peaks correlating the ^{1}H chemical shift 0-3 ppm (CH_3) and the naphthyl carbon peaks in the range of 120-140 ppm suggest that the inter/intra-

molecular proximities between the quaternary carbon atoms and the CH_3 groups are perturbed in the glassy phase, as shown by the dashed red box in the lower half of Figure 3c as compared to the analogous peaks for the crystal (Figure 2c). The loss of interaction between the alkyl protons and naphthyl carbon atoms further aligns with the absence of 2D peaks between alkyl carbon atoms (10-40 ppm) and the aromatic protons (6-8 ppm), as depicted by dashed red boxes in the upper half. However, strong intensity but relatively broad 2D peaks associated with the naphthyl groups (120-145 ppm) are observed, confirming that the glassy phase largely results from the local disorder at the organic-inorganic interface, caused by the conformational disorder in the tethering groups and the weak non-covalent interactions between the $PbBr_6$ octahedra and spacer cations.

To gain further insights into the local dynamics of spacer cations, we have carried out 2D cross-polarization variable contact (CP-VC) experiments. The CP-VC NMR approach has been previously applied to probe the rotational dynamics of aromatic rings in layered 2D perovskites.[41] The 2D $^{13}C\{^1H\}$ CP-VC experiment (Figure S6a) is a ^{13}C-^1H dipolar-coupling-mediated measurement that correlates ^{13}C chemical shifts in the horizontal axis with the dipolar coupling values of the directly bonded C-H moieties in the vertical axis. For glass S-NPB, the measured $D_{CH} = 22.1$ kHz is closer to the theoretical value of 23 kHz associated with a rigid C-H bond, indicating the restricted molecular motion of naphthyl rings. In addition, broad features of proton signals associated with NH_3 and CH_3 peaks (Figure S6b), further corroborate the restricted dynamics of the tethered groups at the organic/inorganic interface. FTIR spectroscopy analysis performed on the crystalline and glassy SNPB samples (see Experimental Section) supports the assertion of weaker non-covalent (i.e., hydrogen bonding) interaction at the organic-inorganic interface in the glassy state, as evident from the heightened intensity of the N-H stretching mode (3460 cm^{-1}) in this state (Figure 4).[75] This mode is characteristic of relatively free N-H groups, as opposed to the vibration modes appearing at lower wavenumbers, typically observed for more strongly hydrogen bonded N-H groups.[75, 76] The lower wavenumber N-H modes are largely swamped in the shoulder of the broad spectral feature near 3000 cm^{-1} (primarily associated with C-H stretching modes)[77] for the current crystalline and glassy samples (Figure 4), as for the crystalline iodide analog.[78] Loss of conformational order at the organic-inorganic interface, as indicated in the current study, supports the recent observation of the loss of circular dichroism (CD) signal at wavelengths corresponding to absorption from the inorganic framework—i.e., pointing to the loss of chiral

transfer from the organic cation to the inorganic framework in the glass—as recently reported by Zhao et al.[54]

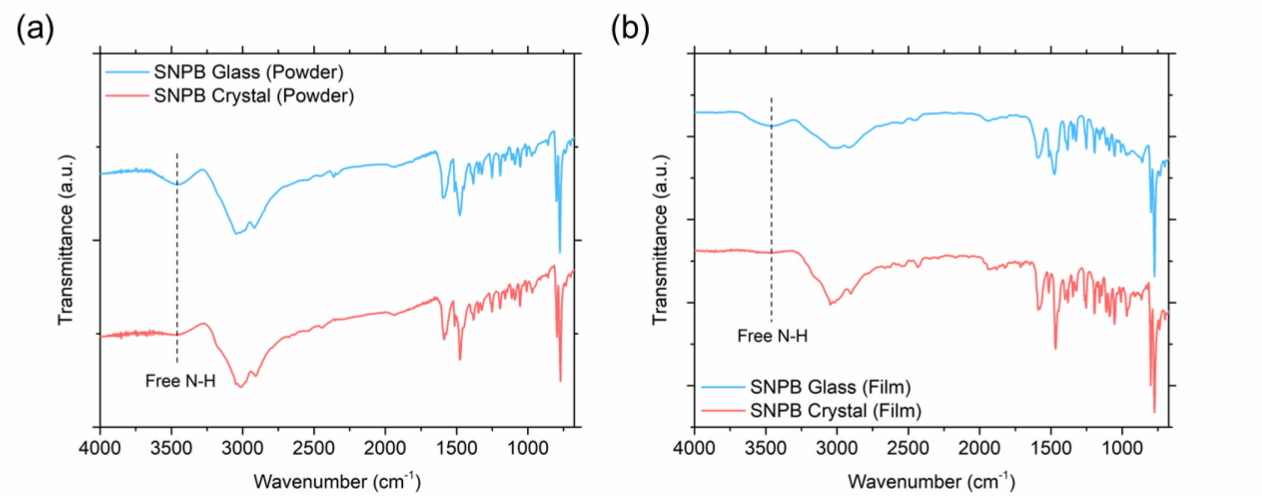

Figure 4. Fourier transform infrared (FTIR) spectroscopy of crystalline and glassy samples of SNPB. The patterns for both the crystalline and glassy (a) powdered and (b) film samples are similar except for a difference in enhanced intensity for the absorbance corresponding to relatively free 'N-H' stretching mode at 3460 cm^{-1}.[75] The magnified view of the FTIR fingerprint region (up to 1700 cm^{-1})[79] for the organic component shows no significant differences (Figure S7).

The local structure of crystalline, melt, and glassy SNPB was further characterized through in-situ temperature dependent X-ray diffraction (XRD) (Figure 5; also, see Experimental Section) of SNPB films. The presence of a broad diffraction feature peaking at 5.7° corresponding to an average d-spacing of ~15 Å points to maintaining some degree of the layered ordering in both the melt and glass states (Figure 5), albeit with a reduction in the layer spacing (i.e., the crystalline peak at 4.6° corresponds to a d-spacing of ~19 Å). The change in d-spacing presumably arises from the disordering and rearrangement in the organic cation tethering groups, possibly accompanied by tilting of the naphthyl groups. The XRD peak width in glass/melt corresponds to a correlation length of 4-5 nm and thus the order is limited to a few layers. Recently, we have presented a second example of a glass-forming MHP with much faster glass-crystal transition kinetics, and also pointed out the possibility of and impact of slight changes of stoichiometry during heat cycling.[80] In the current study, organic loss was inhibited by utilizing a Kapton overlayer to cover the film during elevated temperature XRD measurement. We can't exclude the

possibility that some of the extra peak broadening in the melt phase data (relative to that for the glass) may arise due to limited sample degradation at the relatively high measurement temperature. Indeed, intentionally holding the sample at 190 °C for extended time (exceeding 10 min) leads to formation of a $PbBr_2$ secondary phase within the sample (Figure S8). Nevertheless, the ability to recover the original d-spacing upon crystallizing the glass film (Figure 5) implies that the decrease in interlayer spacing in the melt/glass states does not arise from changes in composition. The weak layering we observe suggests analogies to turbostratic-like order seen in carbon and other layered materials[61, 62] or to glass-like liquid crystalline structure observed in quenched small molecules.[60]

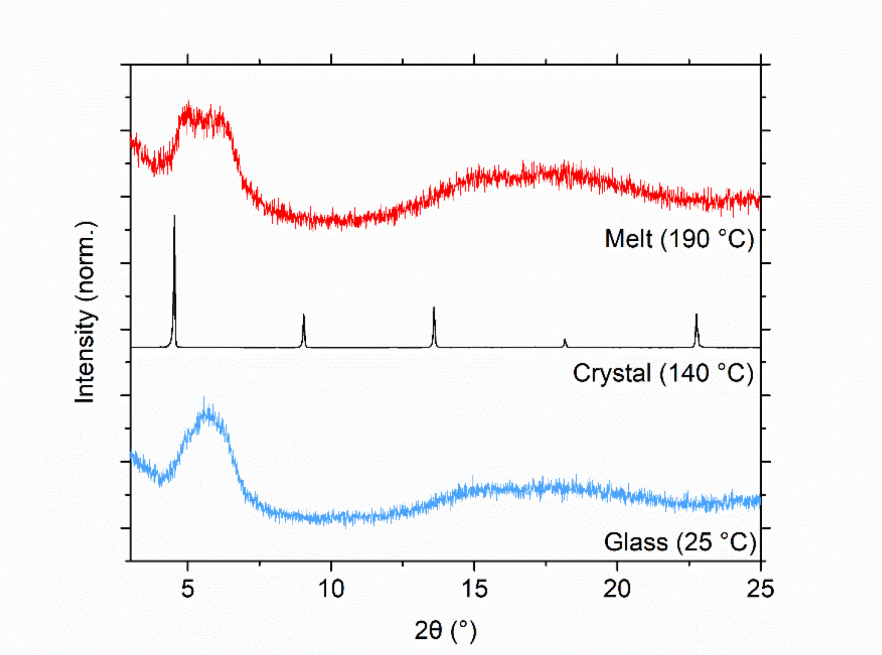

Figure 5. The in-situ temperature-dependent x-ray diffraction (XRD) pattern of glassy, crystalline, and molten SNPB films recorded at various temperatures. The broad peak near 2θ of 5.7° in the glass and melt states of SNPB reveals the amorphous nature, devoid of the long-range ordering observed in crystalline SNPB that instead shows a family of repeating 00l peaks. Additionally, the original d-spacing corresponding to 19 Å (2θ ~4.6°) is re-established in the recrystallized film, suggesting its successful reversion to the parent crystalline composition.

Pair distribution function (PDF) analysis from X-ray total scattering provides local order insights related to the inorganic sublattice of SNPB, as a result of the larger X-ray scattering strengths (atomic form factors) of Pb and Br compared to the C, N, and H atoms in the naphthylethylammonium cation. Here, the PDF analysis provides information on nearest neighbor

Pb-Br coordination environments and extended correlations in real space. The reduced pair distribution function *G(r)* (Figure 6a) describes the real space distance between atom pairs and the extent of structural coherence as oscillations about $G(r) = 0$. The PDF of crystalline SNPB displays structural correlations beyond 30 Å in real space, expected for the ordered, periodic structure (Figure S9). In contrast, the glass and melt states of SNPB lack discernible *G(r)* peaks beyond 8-10 Å, and thus long-range order, even across neighboring $PbBr_6$ octahedra, is largely absent in these states. Short range correlations, however, are qualitatively similar across all three states, with broadened peaks in the glass predominantly due to static disorder and primarily due to thermal broadening for the melt state (measured at 195 °C). The general similarity in the PDF pattern suggests that the short-range structural motif of corner-sharing $PbBr_6$ is largely maintained in the glass and melt states, consistent with the Raman and ss-NMR results. The retention of short-range order in glassy SNPB also aligns with the recent findings on a ball-milling-induced amorphous SNPB state,[81] as well as with previous findings in materials including MOFs[82, 83] and dicyanamide based organometallic perovskites. [46]

From *G(r),* we calculate the radial distribution function, *R(r*), for which integrated peak areas are expected to be proportional to coordination number. Figure 6c shows a Z-weighted histogram of pair distances from the ambient temperature crystal structure of SNPB[30] overlaid with pair-wise *R(r)/r* to visualize the sum of atom pairs comprising each peak. For crystalline SNPB, the first peak centered at approximately 3 Å represents the Pb-Br bond distances of the $PbBr_6$ octahedra. However, the Pb-Br bond lengths are asymmetrically distributed due to the distorted $PbBr_6$ octahedra (Figure 6b), with an observable shoulder on the right side of the Pb-Br peak, corresponding to a single elongated bridging Pb-Br bond length (Figure 6c). The second peak at approximately 4.2 Å represents a broad range of Br-Br distances along edges of the octahedra. Finally, the peak centered near 6 Å primarily represents the Pb-Pb pair for neighboring octahedra, amid less significant contributions from Br-Br and higher order Pb-Br pairs.

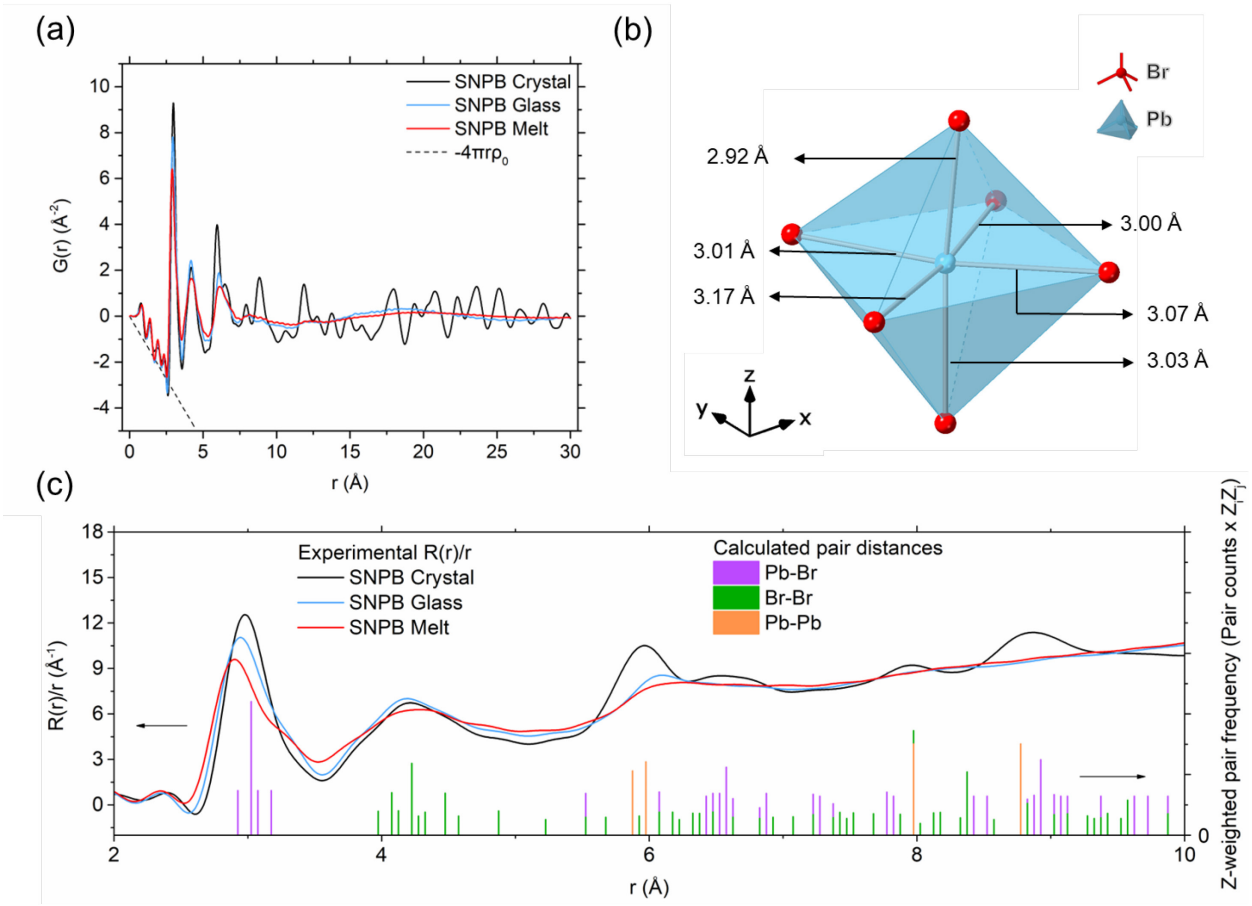

Figure 6. (a) Reduced pair distribution function (PDF) of SNPB plotted between 0 and 30 Å for crystalline, melt, and glass states. The dashed black line depicts the sloping baseline ($-4\pi r\rho_0$) (see Experimental Section) to obtain the function R(r)/r. (b) Distorted $PbBr_6$ octahedron in crystalline SNPB showing Pb-Br bond lengths. (c) Expanded region of R(r)/r showing the Pb-Br, nearest Br-Br, Pb-Pb and Pb-Br (next nearest) pair correlations compared against a histogram of pair distances scaled in proportion to the product of each pairs' atomic numbers: Z_iZ_j. Crystal and glass data are collected at RT, while the melt is at 195 °C. Note the strong similarity between the melt and glass G(r) and F(Q) (Figure S10) showing structural congruence for the Pb-Br octahedra in these states.

The respective *R(r)* peaks of the glassy state represent a marked departure from the local order of the crystal. The Pb-Br peak broadens compared to the crystalline state, implying an overall wider distribution of Pb-Br bond lengths within the glass. In addition, the right side of the peak (r ≈ 3.2 Å) displays a shoulder that increases in intensity for glass and melt phases. Accompanied by a reduction in overall peak amplitude, these changes show a subset of Pb-Br bond lengths increase

in the disordered SNPB states compared to the crystalline state, consistent with narrow and broad ^{207}Pb NMR shifts observed for the crystalline and glassy states respectively (Figures S4). To quantify changes in the Pb-Br bond length distribution and test for significant changes in Pb-Br coordination number ($CN_{Pb\text{-}Br}$), we fit a simple model to the *R(r)* peak comprised of two overlapping Gaussian line shapes (Figure S11, Table S2) and a linear approximation of neighboring peak overlap at higher *r* values. We take the total Pb-Br peak area as the sum of the two optimized Gaussians. With respective *R(r)* peak areas proportional to coordination number and with $CN_{Pb\text{-}Br}$ known in the crystalline state, we normalize this total peak area to six for the crystal ($CN_{Pb\text{-}Br\ Norm.}$) and apply this scale factor to glass and melt phases (Table S2). Using this approach, we find $CN_{Pb\text{-}Br\ Norm.}$ values for crystal (6.0 ± 0.7), glass (6.2 ± 0.4**),** and melt (6.1 ± 0.3) phases that remain the same within standard error. We may also compare the relative areas of the two optimized Gaussian peaks for insight into the distribution of Pb-Br bond lengths. As the total area of these two peaks is effectively constant, the change in peak area ratio in the crystal (1.8) relative to the glass (1.0) phase further support the increase in a subset of Pb-Br bond lengths upon amorphization, even amidst the overall broader distribution in the glass relative to the crystal (Figure S10, Table S2).

One possibility in transitioning from a solid crystal to a melt would be for the $PbBr_4^{2-}$ sheets to partially break apart during the melting process, with this structural aspect locked in during the quenching process to form the glass, which would effectively create Pb-Br-based islands still nominally sandwiched between the bilayers of organic cations and including disorder among the tethering groups. Introducing breaks in the Pb-Br bonding (i.e., effectively "cuts" in the $PbBr_4^{2-}$ sheets) would necessitate, to maintain the overall $PbBr_4^{2-}$ stoichiometry, either reducing the coordination of some Pb atoms at the edges of the islands to a value <6 (if corner-sharing is maintained) or changing the connectivity among some of the octahedra at the island edges to an edge- or face-sharing motif (if maintaining octahedral coordination).[84] The above $CN_{Pb\text{-}Br}$ analysis supports the hypothesis that the bulk of the Pb atoms within the glass/melt maintain nominal 6-fold (i.e., octahedral) coordination. In terms of possible change in connectivity from corner-sharing to edge- or face-sharing, a significant change in higher order (r ≳ 4 Å) PDF peak shapes would be expected in either case (Figure S12)—i.e., departure from corner-sharing connectivity should be distinguishable by Pb-Pb distances decreasing from 6 Å to ~4-5 Å in face- or edge-sharing connectivity. In the PDF, for a change in connectivity, we would expect both i) an increase in

amplitude near 4.2 Å and ii) a decrease in amplitude near 6 Å as the Pb-Pb distance becomes nearly commensurate with Br-Br. Given the lack of significant changes in the 4.2 Å peak shape between crystal and glass states (Figure 6c), we surmise that there are no significant new additional Pb-Pb contributions at this distance range. Considering the increased damping of PDF oscillations and loss of structural coherence at longer length scales, confident analysis of the 6 Å peak becomes increasingly difficult. However, the differences in this peak, especially clear in the *G(r)* plot (Figure 6a), appear consistent with expected disorder/damping, without significant changes in weighting among the components of the peak. Given these points, we conclude that corner-sharing $PbBr_6$ octahedra remain the dominant motif upon melting/vitrification, although the analysis does not preclude small changes in coordination/connectivity below the detection limits of the analysis. Overall, the PDF results support the hypothesis that loss of structural correlation in the glass/melt states arises principally from disordering of hydrogen bonding at the $PbBr_4^{2-}$-organic cation interface, as also highlighted from the discussion related to the other analysis approaches.

Finally, the transformation of the crystalline SNPB into a glassy state, marked by the loss of long-range periodicity, has significant implications. Specifically, the loss of coherence beyond ~10 Å with local changes in the inter- and intra-octahedra distortion may, in part, contribute to a blue shift of (~ 50 nm or 0.4 eV) in the absorption onset of the glassy state, when compared with the ordered and extended inorganic lattice found in the crystalline counterpart (data reproduced from the earlier work as Figure S13).[44] Recent reports on photoluminescence of the crystalline and glassy state of RNPB (another enantiomeric form of SNPB),[50] and ball-milling-induced amorphous SNPB,[75] also corroborates the blue shift behavior wherein the glassy state fluorescence is bluish in color whereas the crystalline state is more on the warm white side. A significant decrease of two orders in electrical conductivity along the lateral direction has also been documented,[54] which can be, at least in part, attributed to the loss of periodicity within the inorganic sub-lattice due to disorder in inter-octahedra bond angles or perhaps Pb-Br bond lengthening within the inorganic layer.

Conclusion

In summary, our study represents the first comparison of the local structure within a molten and glassy MHP (relative to the crystalline state), achieved through a comprehensive integration of Raman spectroscopy, solid-state NMR, FTIR, and XRD coupled with PDF measurements.

Contrasting the crystalline state of SNPB with its glassy counterpart reveals intriguing differences: The crystalline state demonstrates Raman polarization dependence and distinct modes, whereas the glassy state exhibits an absence of polarization dependency and shows broad Raman features (within a similar wavenumber regime), as expected for the absence of long-range periodicity in a glass. Notably, ^{1}H, ^{13}C, ^{14}N, and ^{207}Pb ss-NMR chemical shifts and associated 2D correlation spectra confirm that substantial disruptions appear within the tethering ammonium group and the associated dihedral angles linking the naphthyl and ammonium groups for the glassy state. These disruptions are pivotal factors contributing to the loss of order at the organic-inorganic interface, as also evidenced by the emergence of relatively free (weakly hydrogen bonded) N-H stretching modes in the FTIR spectrum. Our study also demonstrates the preservation of registry among the naphthyl groups (presumably associated with significant cation-cation interactions), leading to the retention of some layered structural order in melt and glassy SNPB, as revealed from the in-situ XRD. Moreover, the PDF analysis supports the dominant presence of corner-sharing among the octahedra in the glassy state, with an atomic correlation length of 8-10 Å, beyond which there is a breakdown of coherence. This breakdown may be attributable to disorder in inter-octahedra bond angles. The molten state also exhibits a similar broad Raman feature and structural correlation length, suggesting a similar local structure to that of glass. The combined results indicate that the exemplary glassy perovskite under study might aptly be termed a "perovskite glass" (given that it maintains some features of the crystalline perovskite structure, including dominant corner-sharing among lead bromide octahedra). The alterations in the local structure of the glass correlate with previously observed changes in optoelectronic properties, including decreased electrical conductivity and a blue shift in the optical absorption profile. These findings aid in comprehending the structural distinctions among different states of MHPs and shed light on the structure induced property changes that can be leveraged in the development of next generation energy storage, memory and computing devices.

AUTHOR INFORMATION

*Corresponding Author

David B. Mitzi – Email: david.mitzi@duke.edu ; orcid.org/0000-0001-5189-4612;

G. N. Manjunatha Reddy – Email: gnm.reddy@univ-lille.fr ; orcid.org/0000-0002-8283-2462

EXPERIMENTAL SECTION

Methods:

1. Materials:

(*S*)-(−)-1-(1-naphthyl)ethylamine (>99%, Sigma Aldrich), lead bromide ($PbBr_2$, 99.99%, TCI chemicals), hydrobromic acid (HBr) (48 wt% in H_2O, >99.99%, Sigma Aldrich), and N,N-dimethylformamide (DMF) (anhydrous, 99.8%, Sigma Aldrich) were procured and used without further purification.

2. Crystal synthesis:

To grow crystals of $(S\text{-}NEA)_2PbBr_4$ perovskite crystals (henceforth referred as SNPB), where S-NEA refers to (*S*)-(−)-1-(1-naphthyl)ethylammonium, stoichiometric amounts of $PbBr_2$ (180 mg, 0.48 mmol) and (*S*)-(−)-1-(1-naphthyl)ethylamine (156 µL, 0.96 mmol) were dissolved in aq. HBr (2.0 mL) and deionized water (4.8 mL) in a vial at 95 °C. The hot solution was slowly cooled to 20 °C over a period of 24 hours in a water bath, resulting in the formation of colorless plate-like SNPB single crystals. The as-obtained crystals of SNPB were filtered and washed three times with diethyl ether before final vacuum drying and storage for further use.

3. Preparation of glassy SNPB:

Soda-lime glass substrates (25.4 × 10.0 × 1.2 mm^3) were first washed under running deionized water and then cleaned by ultrasonication in acetone and isopropyl alcohol for 3 min each, followed by air drying. A few single crystals (<1.0 mg) of SNPB perovskite were placed on a soda lime glass substrate and the substrate was then placed on a hot plate set to 190 °C (exceeding the melting point by ~15 °C to reduce melt viscosity); the structure was pressed on top with another preheated soda lime glass substrate to spread the melt. After visual inspection to ensure melting (≈60 s), the sandwiched glass was left to heat for another 30 s before quickly placing on a metallic steel bench to rapidly cool to room temperature for glass formation. The glassy SNPB, sandwiched between soda-lime glass substrates, was scratched using a spatula to obtain powdered glassy SNPB to facilitate various characterizations, after removing the top soda lime glass slide. For in-situ X-ray diffraction (XRD) measurements, the SNPB glassy films were prepared using the above

method, with the only exception being an additional 8-micron Kapton sheet placed between the two soda lime glass substrates to provide protection against significant decomposition during measurement at elevated temperatures.

4. Raman spectroscopy:

Raman scattering measurements were performed using a custom-built back-scattering system (Figure S1).[85, 86] A below band-gap 1.58 eV continuous-wave pump-diode laser from Toptica Inc. (USA) was employed as the excitation source. The incident beam was linearly polarized using a Glan-laser polarizer from Thorlabs (USA) and directed into a microscope (Zeiss, USA). A 0.55 NA/50x objective (Zeiss, USA) was used to focus the laser beam onto the sample. To control the excitation polarization, a zero-order half-wave plate (Thorlabs, USA) was utilized, allowing small increments (2.5 degrees) of rotation between consecutive spectra in the polarization-orientation (PO) measurement. The back-scattered beam, collected by the objective, was then passed through another polarizer to selectively collect light scattered parallel or perpendicular to the incident polarization. To minimize Rayleigh scattering, the beam passed through a volume holographic beam-splitter and two notch filters (OD > 4) from Ondax Inc. (USA). Subsequently, the beam was focused onto a 1 m long spectrometer (FHR 1000, Horiba) and dispersed by either a 1800 gr/mm or a 600 gr/mm grating. A silicon CCD detector from Horiba Inc. (USA) captured the dispersed light. For temperature control, the crystals were mounted in an optical cryostat (Janis Inc., USA), cooled by either liquid nitrogen or liquid helium. Unpolarized spectra were obtained by summing the spectra measured for all incident polarizations, collected in parallel and perpendicular configurations. These spectra were then normalized to the maximum intensity.

For temperature-dependent measurements, the SNPB samples (crystalline and glassy form) were glued onto a cryostat plate with silver paste. The cryostat was then pumped to vacuum conditions ($\sim 10^{-5}$ mbar). Afterwards, the temperature was ramped between two consecutive measurements at 2 °C/min and allowed to equilibrate for 10-15 minutes upon reaching the required temperature before measurement. To obtain a valid comparison between the glass, crystal and melt states, reduced Raman spectra were obtained by dividing the raw Raman spectra of each state at different temperatures (glass, crystal, and melt state, measured at T = 345 K, 446 K, and 458 K, respectively) by the temperature-dependent, one-phonon Bose-Einstein distribution that represents the phonon population with temperature (Figure 1d).[64, 65]

5. Solid-state nuclear magnetic resonance (ss-NMR) spectroscopy:

For all solid-state nuclear magnetic resonance (ss-NMR) measurements, the crystalline and glassy SNPB materials were packed into 1.3 mm (outer diameter) cylindrical zirconia rotors fitted with Vespel® caps. All 1D ^{1}H and ^{13}C{^{1}H} CP-MAS, and 2D ^{1}H-^{207}Pb and ^{1}H-^{13}C correlation NMR experiments were conducted on a Bruker AVANCE NEO (18.8 T, Larmor frequencies were ^{1}H = 800.1 MHz, ^{13}C = 201.3 MHz and ^{207}Pb = 167.4 MHz) spectrometer with a 1.3 mm H-X probehead operating at ambient temperature. Unless otherwise stated, the magic-angle spinning (MAS) was set to 50 kHz in all measurements. The ^{1}H and ^{13}C experimental shifts were calibrated with respect to neat TMS using adamantane as an external reference (higher ppm ^{13}C resonance, 35.8 ppm, and the ^{1}H resonance, 1.85 ppm).

For crystalline and glassy SNPB materials, the 1D ^{1}H MAS spectra were acquired by co-adding 32 transients using a delay of 2.5 seconds. 1D ^{1}H→^{13}C CP-MAS spectra were acquired with 2048 co-added transients with short (0.2 ms) and long (4 ms) CP contact times. The ^{1}H-detected 2D ^{1}H–^{13}C heteronuclear correlation (HETCOR) spectra were acquired with 128 t_1 increments, each with co-addition of 32 transients. The 1D ^{1}H{^{14}N} heteronuclear multiple-quantum correlation (HMQC)-filtered ^{1}H spectra were acquired with 32 co-added transients. The 2D ^{1}H-^{14}N dipolar (*D*)-HMQC NMR spectra were acquired with SR4 recoupling to reintroduce the heteronuclear ^{14}N-^{1}H dipolar couplings with a duration of 160 μs. For each of the 64 t_1 increments, acquired using the States-TPPI method, a rotor synchronized increment of 20 μs was used. 4 transients were co-added with a recycle delay of 3 s. The ^{1}H-^{1}H Double-Quantum–Single-Quantum (DQ-SQ) correlation spectra were acquired with Back-to-Back (BaBa) pulse sequence using DQ recouping time of 20 μs, corresponding to one rotor period. The 2D spectra were obtained by co-addition of 128 rotor synchronized t_1 increments, each with 16 transients. All 2D ^{1}H-detected ^{1}H–^{207}Pb HETCOR spectra were acquired at fast MAS (50 kHz) with 48 t_1 increments, each with 512 co-added transients, using 6 ms of CP contact time. All 1D and 2D ssNMR spectra were processed with the built-in Bruker Topspin 4.1.1 package.

6. Fourier transform infrared (FTIR) spectroscopy:

FTIR measurements were made using Thermo Electron Nicolet 8700 instrument. A few micrograms of the crystalline and glassy SNPB powder were freshly prepared and mixed with KBr to form a pressed pellet for measurement under transmission mode. The FTIR measurements on

glassy and crystalline films (obtained through recrystallization of glassy films at 140 °C on a hotplate) were carried out under attenuated total reflectance (ATR) mode.

7. In-situ temperature dependent X-ray diffraction (XRD):

An in-situ temperature dependent XRD measurement was performed on a pre-prepared SNPB glassy film with an 8-micron overlayer of Kapton sheet using an Anton Paar XRDynamic 500 with HTK 1200N Stage. The sample was measured over the 3 - 25° 2θ range at various temperatures. Initially, the glassy sample was measured at 25 °C (room temperature), then heated to 140 °C at a ramp rate of 10 °C/min and held at this temperature for 5 minutes to allow crystallization of the sample. Subsequently, a measurement was performed in the crystalline state. Following this, the XRD stage was ramped to 190 °C at a ramp rate of 10 °C/min and held for 1 minute to ensure the melting of the crystalline film. Another measurement was then conducted to obtain the XRD spectrum in the melt state (Figure 5).

8. Pair Distribution Function (PDF) analysis:

Data collection and reduction:

X-ray total scattering data were collected on APS 11-ID-B at the Argonne National Laboratory. Scans were collected over 180s for each sample at 58.7 keV incident X-ray energy. Samples were sealed in quartz capillaries and loaded into a Linkam stage for elevated temperature control.

Background scattered intensity was subtracted from each azimuthal integration *I(Q)*. The reduced PDF was calculated from *I(Q)* using PDFgetX3 using the ad hoc reduction to *F(Q)* and subsequent sine Fourier transformation to *G(r)*.[87] The average scattering factor $\langle f(Q) \rangle$ for each SNPB state is taken as the crystal phase elemental composition: $C_{24}H_{28}N_2PbBr_4$. PDFgetX3 input parameters used to generate *G(r)* are listed in Table S1.

$$F(Q) = Q\left[\frac{I(Q) - \langle f(Q)^2 \rangle + \langle f(Q) \rangle^2}{\langle f(Q) \rangle^2} - 1\right]$$

$$G(r) = \left(\frac{2}{\pi}\right)\int_{Q_{min}}^{Q_{max}} F(Q)sin(Qr)dQ$$

Radial distribution function analysis:

From experimentally obtained *G(r)* we perform a conversion to the Radial Distribution Function *R(r)* using the average atomic density of crystalline SNPB: $\rho_0 = 0.0871$ atoms/Å^3 to calculate the linear baseline underlying *G(r)*.

$$R(r) = r[G(r) + 4\pi r\rho_0]$$

Note: As the histogram distances in manuscript Figure 6c are calculated pair-wise (not with respect to an origin) we plot the representative form *R(r)/r* with this histogram.

To analyze coordination number and the distribution of Pb-Br bond lengths we fit and calculate the integrated area of *R(r)* peaks centered at approximately 3 Å. Although this peak is the summation of partial contributions from six unique Pb-Br nearest neighbor distances in the crystal structure, we fit a simplified model comprising two Gaussian line shapes and a linear approximation of trailing edge peak overlap, which produces an adequate fit to the experimental data (Figure S9, Table S2). Peak parameters are optimized using a non-linear least squares method. Due to the imperfect scale of *G(r)* obtained experimentally, the total integrated area of the crystalline peak is then normalized to the assumed average Pb-Br coordination number of six, and this same scale is applied to glass and melt phases. All fitted parameters and calculated areas are reported in Table S2. Errors in Gaussian and linear fit variables are calculated from the covariance of the eight parameters fit simultaneously. Errors in the integrated area of these peaks are obtained via resampling a normal distribution of the Gaussian peak amplitude and width with calculated standard error. We note that there is a degree of systematic error introduced in the *G(r)* to *R(r)* conversion by assuming the atomic density, ρ_0, of each phase is the same as that of the crystalline phase. As disordered phases realistically have lower atomic density than the crystal, this source of error would be consistent with the slight increase in total peak area found for the glass and melt. For the melt phase especially, additional thermal broadening and increased peak overlap hinders confident interpretation of this data. We draw qualitative conclusions for the melt phase, although fit results are generally consistent with expected high temperature behavior and similar to the glass phase results.

ACKNOWLEDGEMENT

This work was supported by the National Science Foundation under Grants No. DMR- 2114117 and DMR-2114121. D.M.L acknowledges support from a National Science Foundation Graduate Research Fellowship under Grant No. DGE 2040434. O.Y. acknowledges funding from ISF(209/21) and from the European Research Council (850041 -ANHARMONIC) for the Raman spectroscopy study. Support from the EU H2020 research and innovation programme under the Marie Skłodowska-Curie grant (No. 795091) and INFRANALYTICS FR-2054 CNRS France is acknowledged for conducting ssNMR measurements. X-ray total scattering experiments used resources of the Advanced Photon Source, a U.S. Department of Energy (DOE) Office of Science user facility operated for the DOE Office of Science by Argonne National Laboratory under Contract No. DE-AC02-06CH11357. The work was performed in part at the Duke University Shared Materials Instrumentation Facility (SMIF), a member of the North Carolina Research Triangle Nanotechnology Network (RTNN), which is supported by the National Science Foundation (Grant ECCS-2025064) as part of the National Nanotechnology Coordinated Infrastructure.

ASSOCIATED CONTENT

Supporting Information

Scheme of the polarization-orientation (PO) Raman scattering measurements, Temperature-dependent Raman spectra of crystalline and glassy SNPB, Solid-state 1D $^{13}C\{^{1}H\}$ CP-MAS NMR spectra of crystalline and glassy SNPB, Solid-state 1D ^{207}Pb NMR spectrum of crystalline and glassy SNPB, Solid-state 2D ^{1}H-^{14}N NMR spectra, along with 2D ^{1}H-^{1}H Double-Quantum – Single-Quantum (DQ-SQ) correlation spectra of SNPB crystal and SNPB glass, Fourier transform infrared (FTIR) spectroscopy of crystalline and glassy samples of SNPB, Pair distribution function (PDF) of crystalline and glassy SNPB along with calculated PDF pattern, PDFgetX3 Fourier Transform Parameters, Total X-ray scattering or PDF of SNPB in the glass and melt states, Simple model fitting on experimental R(r) functions for crystal, glass, and melt states of SNPB, Optimized fit parameters from model fitting on experimental R(r) functions for crystal, glass, and melt states of SNPB, Atomic pair distance histograms for corner-, edge-, and face-shared $PbBr_6$ octahedra connectivity, UV–vis absorbance spectroscopy of glassy SNPB perovskite films.

REFERENCES

1. Min, H.; Lee, D. Y.; Kim, J.; Kim, G.; Lee, K. S.; Kim, J.; Paik, M. J.; Kim, Y. K.; Kim, K. S.; Kim, M. G., Perovskite solar cells with atomically coherent interlayers on SnO2 electrodes. *Nature* **2021,** *598*, 444-450.
2. Best Research-Cell Efficiency Chart, https://www.nrel.gov/pv/cell-efficiency.html (accessed: November 2023.
3. Jiang, J.; Chu, Z.; Yin, Z.; Li, J.; Yang, Y.; Chen, J.; Wu, J.; You, J.; Zhang, X., Red Perovskite Light-Emitting Diodes with Efficiency Exceeding 25% Realized by Co-Spacer Cations. *Adv. Mater.* **2022,** *34*, 2204460.
4. Li, G.; Wang, Y.; Huang, L.; Sun, W., Research progress of high-sensitivity perovskite photodetectors: A review of photodetectors: Noise, structure, and materials. *ACS Appl. Electron. Mater.* **2022,** *4*, 1485-1505.
5. Sakhatskyi, K.; Turedi, B.; Matt, G. J.; Wu, E.; Sakhatska, A.; Bartosh, V.; Lintangpradipto, M. N.; Naphade, R.; Shorubalko, I.; Mohammed, O. F.; Yakunin, S.; Bakr, O. M.; Kovalenko, M. V., Stable perovskite single-crystal X-ray imaging detectors with single-photon sensitivity. *Nat. Photonics* **2023,** *17*, 510-517.
6. Liu, F.; Wu, R.; Wei, J.; Nie, W.; Mohite, A. D.; Brovelli, S.; Manna, L.; Li, H., Recent progress in halide perovskite radiation detectors for gamma-ray spectroscopy. *ACS Energy Lett.* **2022,** *7*, 1066-1085.
7. Vinattieri, A.; Giorgi, G., Halide perovskites for photonics: recent history and perspectives. In *Halide Perovskites for Photonics*, AIP Publishing LLC Melville, New York: **2021**; pp 1-1-1-28.
8. Mitzi, D. B.; Chondroudis, K.; Kagan, C. R., Organic-inorganic electronics. *IBM J. Res. Dev.* **2001,** *45*, 29-45.
9. Mitzi, D. B., Synthesis, structure, and properties of organic-inorganic perovskites and related materials. *Prog. Inorg. Chem.* **1999,** *48*, 1-121.
10. Saparov, B.; Mitzi, D. B., Organic–inorganic perovskites: structural versatility for functional materials design. *Chem. Rev.* **2016,** *116*, 4558-4596.
11. Mao, L.; Stoumpos, C. C.; Kanatzidis, M. G., Two-dimensional hybrid halide perovskites: principles and promises. *J. Am. Chem. Soc.* **2018,** *141*, 1171-1190.
12. Hay, J. N.; Shaw, S. J., Organic-inorganic hybrids–the best of both worlds? *Europhys. News* **2003,** *34*, 89-92.
13. Dunlap-Shohl, W. A.; Zhou, Y.; Padture, N. P.; Mitzi, D. B., Synthetic approaches for halide perovskite thin films. *Chem. Rev.* **2018,** *119*, 3193-3295.
14. Mitzi, D. B., Templating and structural engineering in organic–inorganic perovskites. *J. Chem. Soc., Dalton Trans.* **2001**, 1-12.
15. Wang, S.; Mitzi, D. B.; Feild, C. A.; Guloy, A., Synthesis and characterization of [NH2C (I): NH2] 3MI5 (M= Sn, Pb): stereochemical activity in divalent tin and lead halides containing Single. ltbbrac. 110. rtbbrac. Perovskite sheets. *J. Am. Chem. Soc.* **1995,** *117*, 5297-5302.
16. Mitzi, D.; Wang, S.; Feild, C.; Chess, C.; Guloy, A., Conducting layered organic-inorganic halides containing〈110〉-oriented perovskite sheets. *Science* **1995,** *267*, 1473-1476.
17. Mitzi, D. B.; Feild, C.; Harrison, W.; Guloy, A., Conducting tin halides with a layered organic-based perovskite structure. *Nature* **1994,** *369*, 467-469.
18. Calabrese, J.; Jones, N.; Harlow, R.; Herron, N.; Thorn, D.; Wang, Y., Preparation and characterization of layered lead halide compounds. *J. Am. Chem. Soc.* **1991,** *113*, 2328-2330.

19. Kamminga, M. E.; Fang, H.-H.; Filip, M. R.; Giustino, F.; Baas, J.; Blake, G. R.; Loi, M. A.; Palstra, T. T., Confinement effects in low-dimensional lead iodide perovskite hybrids. *Chem. Mater.* **2016,** *28*, 4554-4562.
20. Tremblay, M.-H.; Boyington, A.; Rigin, S.; Jiang, J.; Bacsa, J.; Al Kurdi, K.; Khrustalev, V. N.; Pachter, R.; Timofeeva, T. V.; Jui, N., Hybrid Organic Lead Iodides: Role of Organic Cation Structure in Obtaining 1D Chains of Face-Sharing Octahedra vs 2D Perovskites. *Chem. Mater.* **2022,** *34*, 935-946.
21. Knutson, J. L.; Martin, J. D.; Mitzi, D. B., Tuning the band gap in hybrid tin iodide perovskite semiconductors using structural templating. *Inorg. Chem.* **2005,** *44*, 4699-4705.
22. Du, K.-z.; Tu, Q.; Zhang, X.; Han, Q.; Liu, J.; Zauscher, S.; Mitzi, D. B., Two-dimensional lead (II) halide-based hybrid perovskites templated by acene alkylamines: crystal structures, optical properties, and piezoelectricity. *Inorg. Chem.* **2017,** *56*, 9291-9302.
23. Smith, M. D.; Karunadasa, H. I., White-light emission from layered halide perovskites. *Acc. Chem. Res.* **2018,** *51*, 619-627.
24. Li, T.; Chen, X.; Wang, X.; Lu, H.; Yan, Y.; Beard, M. C.; Mitzi, D. B., Origin of broad-band emission and impact of structural dimensionality in tin-alloyed Ruddlesden–Popper hybrid lead iodide perovskites. *ACS Energy Lett.* **2019,** *5*, 347-352.
25. Shen, W.; Chen, J.; Wu, J.; Li, X.; Zeng, H., Nonlinear optics in lead halide perovskites: mechanisms and applications. *ACS Photonics* **2020,** *8*, 113-124.
26. Jana, M. K.; Song, R.; Xie, Y.; Zhao, R.; Sercel, P. C.; Blum, V.; Mitzi, D. B., Structural descriptor for enhanced spin-splitting in 2D hybrid perovskites. *Nat. Commun.* **2021,** *12*, 4982.
27. Kepenekian, M.; Robles, R.; Katan, C.; Sapori, D.; Pedesseau, L.; Even, J., Rashba and Dresselhaus effects in hybrid organic–inorganic perovskites: from basics to devices. *ACS nano* **2015,** *9*, 11557-11567.
28. Wang, F.; Gao, H.; de Graaf, C.; Poblet, J. M.; Campbell, B. J.; Stroppa, A., Switchable Rashba anisotropy in layered hybrid organic–inorganic perovskite by hybrid improper ferroelectricity. *Npj Comput. Mater.* **2020,** *6*, 183.
29. Siwach, P.; Sikarwar, P.; Halpati, J. S.; Chandiran, A. K., Design of above-room-temperature ferroelectric two dimensional layered halide perovskites. *J. Mater. Chem. A* **2022**, *10*, 8719-8738.
30. Jana, M. K.; Song, R.; Liu, H.; Khanal, D. R.; Janke, S. M.; Zhao, R.; Liu, C.; Vardeny, Z. V.; Blum, V.; Mitzi, D. B., Organic-to-inorganic structural chirality transfer in a 2D hybrid perovskite and impact on Rashba-Dresselhaus spin-orbit coupling. *Nat. Commun.* **2020,** *11*, 4699.
31. Mitzi, D. B.; Dimitrakopoulos, C. D.; Kosbar, L. L., Structurally tailored organic− inorganic perovskites: optical properties and solution-processed channel materials for thin-film transistors. *Chem. Mater.* **2001,** *13*, 3728-3740.
32. Mitzi, D. B., Synthesis, crystal structure, and optical and thermal properties of $(C_4H_9NH_3)_2MI_4$ (M= Ge, Sn, Pb). *Chem. Mater.* **1996,** *8*, 791-800.
33. Xie, Y.; Song, R.; Singh, A.; Jana, M. K.; Blum, V.; Mitzi, D. B., Kinetically Controlled Structural Transitions in Layered Halide-Based Perovskites: An Approach to Modulate Spin Splitting. *J. Am. Chem. Soc.* **2022,** *144*, 15223-15235.
34. Crace, E. J.; Singh, A.; Haley, S.; Claes, B.; Mitzi, D. B., Meltable Hybrid Antimony and Bismuth Iodide One-Dimensional Perovskites. *Inorg. Chem.* **2023,** *62*, 16161-16169.
35. Singh, A.; Crace, E.; Xie, Y.; Mitzi, D. B., Two-dimensional lead-free hybrid perovskite semiconductor with reduced melting temperature. *Chem. Commun.* **2023,** *59*, 8302-8305.
36. Singh, A.; Xie, Y.; Adams, C.; Bobay, B. G.; Mitzi, D. B., Controlling glass forming kinetics in 2D perovskites using organic cation isomers. *Chem. Sci.* **2024,** *15*, 6432-6444.
37. Dahlman, C. J.; Kubicki, D. J.; Reddy, G. M., Interfaces in metal halide perovskites probed by solid-state NMR spectroscopy. *J. Mater. Chem. A* **2021,** *9*, 19206-19244.

38. Raval, P.; Kennard, R. M.; Vasileiadou, E. S.; Dahlman, C. J.; Spanopoulos, I.; Chabinyc, M. L.; Kanatzidis, M.; Manjunatha Reddy, G., Understanding instability in formamidinium lead halide perovskites: kinetics of transformative reactions at grain and subgrain boundaries. *ACS Energy Lett.* **2022,** *7*, 1534-1543.
39. Jiao, H.; Ni, Z.; Shi, Z.; Fei, C.; Liu, Y.; Dai, X.; Huang, J., Perovskite grain wrapping by converting interfaces and grain boundaries into robust and water-insoluble low-dimensional perovskites. *Sci. Adv.* **2022,** *8*, eabq4524.
40. Weadock, N. J.; Sterling, T. C.; Vigil, J. A.; Gold-Parker, A.; Smith, I. C.; Ahammed, B.; Krogstad, M. J.; Ye, F.; Voneshen, D.; Gehring, P. M., The nature of dynamic local order in $CH_3NH_3PbI_3$ and $CH_3NH_3PbBr_3$. *Joule* **2023,** *7*, 1051-1066.
41. Dahlman, C. J.; Kennard, R. M.; Paluch, P.; Venkatesan, N. R.; Chabinyc, M. L.; Manjunatha Reddy, G., Dynamic motion of organic spacer cations in Ruddlesden–Popper lead iodide perovskites probed by solid-state NMR spectroscopy. *Chem. Mater.* **2021,** *33*, 642-656.
42. Lanigan-Atkins, T.; He, X.; Krogstad, M.; Pajerowski, D.; Abernathy, D.; Xu, G. N.; Xu, Z.; Chung, D.-Y.; Kanatzidis, M.; Rosenkranz, S., Two-dimensional overdamped fluctuations of the soft perovskite lattice in CsPbBr3. *Nat. Mater.* **2021,** *20*, 977-983.
43. A. Singh, M. Jana, D. B. Mitzi, US Patent Appl. Pub. No. US 2022/0115593 A1, 2022.
44. Singh, A.; Jana, M. K.; Mitzi, D. B., Reversible Crystal–Glass Transition in a Metal Halide Perovskite. *Adv. Mater.* **2021,** *33*, 2005868.
45. Ma, N.; Horike, S., Metal–organic network-forming glasses. *Chem. Rev.* **2022,** *122*, 4163-4203.
46. Shaw, B. K.; Hughes, A. R.; Ducamp, M.; Moss, S.; Debnath, A.; Sapnik, A. F.; Thorne, M. F.; McHugh, L. N.; Pugliese, A.; Keeble, D. S.; Chater, P.; Garcia, J. M. B.; Moya, X.; Saha, S. K.; A. Keen, D.; Coudert, F.-X.; Blanc, F.; Bennett, T. D., Melting of hybrid organic–inorganic perovskites. *Nat. Chem.* **2021,** *13*, 778–785.
47. Ye, C.; McHugh, L. N.; Chen, C.; Dutton, S. E.; Bennett, T. D., Glass Formation in Hybrid Organic-Inorganic Perovskites. *Angew. Chem. Int. Ed.* **2023,** *135*, e202302406.
48. Zhou, C.; Longley, L.; Krajnc, A.; Smales, G. J.; Qiao, A.; Erucar, I.; Doherty, C. M.; Thornton, A. W.; Hill, A. J.; Ashling, C. W., Metal-organic framework glasses with permanent accessible porosity. *Nat. Commun.* **2018,** *9*, 5042.
49. Gaillac, R.; Pullumbi, P.; Beyer, K. A.; Chapman, K. W.; Keen, D. A.; Bennett, T. D.; Coudert, F.-X., Liquid metal–organic frameworks. *Nat. Mater.* **2017,** *16*, 1149-1154.
50. Bennett, T. D.; Coudert, F.-X.; James, S. L.; Cooper, A. I., The changing state of porous materials. *Nat. Mater.* **2021,** *20*, 1179-1187.
51. Liu, M.; Slavney, A. H.; Tao, S.; McGillicuddy, R. D.; Lee, C. C.; Wenny, M. B.; Billinge, S. J.; Mason, J. A., Designing Glass and Crystalline Phases of Metal–Bis (acetamide) Networks to Promote High Optical Contrast. *J. Am. Chem. Soc.* **2022,** *144*, 22262-22271.
52. Shaw, B. K.; Castillo-Blas, C.; Thorne, M. F.; Gómez, M. L. R.; Forrest, T.; Lopez, M. D.; Chater, P. A.; McHugh, L. N.; Keen, D. A.; Bennett, T. D., Principles of melting in hybrid organic–inorganic perovskite and polymorphic ABX_3 structures. *Chem. Sci.* **2022,** *13*, 2033-2042.
53. Tao, H.; Bennett, T. D.; Yue, Y., Melt-quenched hybrid glasses from metal–organic frameworks. *Adv. Mater.* **2017,** *29*, 1601705.
54. Zhao, Y.; Zhao, J.; Guo, Y.; Zhao, J.; Feng, J.; Geng, Y.; Yang, J.; Gao, H.; Yuan, M.; Jiang, L., Reversible phase transition for switchable second harmonic generation in 2D perovskite microwires. *SmartMat* **2022,** *3*, 657-667.
55. Menahem, M.; Dai, Z.; Aharon, S.; Sharma, R.; Asher, M.; Diskin-Posner, Y.; Korobko, R.; Rappe, A. M.; Yaffe, O., Strongly anharmonic octahedral tilting in two-dimensional hybrid halide perovskites. *ACS nano* **2021,** *15*, 10153-10162.
56. Menahem, M.; Benshalom, N.; Asher, M.; Aharon, S.; Korobko, R.; Hellman, O.; Yaffe, O., Disorder origin of Raman scattering in perovskite single crystals. *Phys. Rev. Mater.* **2023,** *7*, 044602.

57. Raval, P.; Trébosc, J.; Pawlak, T.; Nishiyama, Y.; Brown, S. P.; Reddy, G. M., Combining heteronuclear correlation NMR with spin-diffusion to detect relayed Cl–H–H and N–H–H proximities in molecular solids. *Solid State Nucl. Magn. Reson.* **2022,** *120*, 101808.
58. Laurita, G.; Fabini, D. H.; Stoumpos, C. C.; Kanatzidis, M. G.; Seshadri, R., Chemical tuning of dynamic cation off-centering in the cubic phases of hybrid tin and lead halide perovskites. *Chem. Sci.* **2017,** *8*, 5628-5635.
59. Singh, A.; Mitzi, D. B., Crystallization Kinetics in a Glass-Forming Hybrid Metal Halide Perovskite. *ACS Mater. Lett.* **2022,** *4*, 1840-1847.
60. Bishop, C.; Thelen, J. L.; Gann, E.; Toney, M. F.; Yu, L.; DeLongchamp, D. M.; Ediger, M. D., Vapor deposition of a nonmesogen prepares highly structured organic glasses. *Proc. Natl. Acad. Sci. U.S.A.* **2019,** *116*, 21421-21426.
61. More, R. B.; Bokros, J. C., Biomaterials: carbon. in *Encyclopedia of Medical Devices and Instrumentation*, Second Edition, ed. by Webster, J. G.; John Wiley & Sons, Inc., **2006**; pp. 296-308.
62. Smalley, R. E., Carbon nanotubes: synthesis, structure, properties, and applications. **2003**.
63. Tuschel, D., Why are the Raman spectra of crystalline and amorphous solids different? *Spectroscopy* **2017,** *32*, 26–33-26–33.
64. Walrafen, G.; Fisher, M.; Hokmabadi, M.; Yang, W. H., Temperature dependence of the low-and high-frequency Raman scattering from liquid water. *J. Chem. Phys.* **1986,** *85*, 6970-6982.
65. Shuker, R.; Gammon, R. W., Low-Frequency Vibrational Light Scattering in Viscous Liquids. *J. Chem. Phys.* **1971,** *55*, 4784-4788.
66. Dhanabalan, B.; Leng, Y.-C.; Biffi, G.; Lin, M.-L.; Tan, P.-H.; Infante, I.; Manna, L.; Arciniegas, M. P.; Krahne, R., Directional Anisotropy of the Vibrational Modes in 2D-Layered Perovskites. *ACS Nano* **2020,** *14*, 4689-4697.
67. Yaffe, O.; Guo, Y.; Tan, L. Z.; Egger, D. A.; Hull, T.; Stoumpos, C. C.; Zheng, F.; Heinz, T. F.; Kronik, L.; Kanatzidis, M. G.; Owen, J. S.; Rappe, A. M.; Pimenta, M. A.; Brus, L. E., Local Polar Fluctuations in Lead Halide Perovskite Crystals. *Phys. Rev. Lett.* **2017,** *118*, 136001.
68. Ibaceta-Jaña, J.; Muydinov, R.; Rosado, P.; Mirhosseini, H.; Chugh, M.; Nazarenko, O.; Dirin, D. N.; Heinrich, D.; Wagner, M. R.; Kühne, T. D., Vibrational dynamics in lead halide hybrid perovskites investigated by Raman spectroscopy. *Phys. Chem. Chem. Phys.* **2020,** *22*, 5604-5614.
69. Kubicki, D. J.; Stranks, S. D.; Grey, C. P.; Emsley, L., NMR spectroscopy probes microstructure, dynamics and doping of metal halide perovskites. *Nat. Rev. Chem.* **2021,** *5*, 624-645.
70. Piveteau, L.; Morad, V.; Kovalenko, M. V., Solid-state NMR and NQR spectroscopy of lead-halide perovskite materials. *J. Am. Chem. Soc.* **2020,** *142*, 19413-19437.
71. Franssen, W. M.; Kentgens, A. P., Solid–state NMR of hybrid halide perovskites. *Solid State Nucl. Magn. Reson.* **2019,** *100*, 36-44.
72. Baikie, T.; Barrow, N. S.; Fang, Y.; Keenan, P. J.; Slater, P. R.; Piltz, R. O.; Gutmann, M.; Mhaisalkar, S. G.; White, T. J., A combined single crystal neutron/X-ray diffraction and solid-state nuclear magnetic resonance study of the hybrid perovskites $CH_3NH_3PbX_3$ (X= I, Br and Cl). *J. Mater. Chem. A* **2015,** *3*, 9298-9307.
73. Quarti, C.; Furet, E.; Katan, C., DFT simulations as valuable tool to support NMR characterization of halide perovskites: the case of pure and mixed halide perovskites. *Helv. Chim. Acta* **2021,** *104*, e2000231.
74. Shmyreva, A. A.; Safdari, M.; Furó, I.; Dvinskikh, S. V., NMR longitudinal relaxation enhancement in metal halides by heteronuclear polarization exchange during magic-angle spinning. *J. Chem. Phys.* **2016,** *144*, 224201.
75. Shang, J.; Liu, S.; Ma, X.; Lu, L.; Deng, Y., A new route of CO_2 catalytic activation: Syntheses of N-substituted carbamates from dialkyl carbonates and polyureas. *Green Chem.* **2012,** *14*, 2899-2906.

76. Castañeda, R. l.; Lindeman, S. V.; Krivoshein, A. V.; Metta-Magaña, A. J.; Chen, Y.; Timofeeva, T. V., Remarkable Similarity of Molecular Packing in Crystals of Racemic and Enantiopure 2-Phenylpropionamide: Z'= 4 Structures, Molecular Disorder, and the Formation of a Partial Solid Solution. *Cryst. Growth Des.* **2022,** *22*, 4592-4600.
77. https://www.sigmaaldrich.com/US/en/technical-documents/technical-article/analytical-chemistry/photometry-and-reflectometry/ir-spectrum-table (Accessed November 2023).
78. Ishii, A.; Miyasaka, T., Direct detection of circular polarized light in helical 1D perovskite-based photodiode. *Sci. Adv.* **2020,** *6*, eabd3274.
79. Smith, J. G., Mass spectrometry and infrared spectroscopy. *Organic chemistry* **2011**, 463-488.
80. Singh, A.; Kim, Y.; Henry, R.; Ade, H.; Mitzi, D. B., Study of Glass Formation and Crystallization Kinetics in a 2D Metal Halide Perovskite Using Ultrafast Calorimetry. *J. Am. Chem. Soc.* **2023,** *145*, 18623-18633.
81. Ye, C.; Lampronti, G. I.; McHugh, L. N.; Castillo-Blas, C.; Kono, A.; Chen, C.; Robertson, G. P.; Nagle-Cocco, L. A.; Xu, W.; Stranks, S. D., Mechanochemically-induced glass formation from two-dimensional hybrid organic–inorganic perovskites. *Chem. Sci.* **2024**, *15*, 7198-7205.
82. Qiao, A.; Bennett, T. D.; Tao, H.; Krajnc, A.; Mali, G.; Doherty, C. M.; Thornton, A. W.; Mauro, J. C.; Greaves, G. N.; Yue, Y., A metal-organic framework with ultrahigh glass-forming ability. *Sci. Adv.* **2018,** *4*, eaao6827.
83. Nozari, V.; Calahoo, C.; Tuffnell, J. M.; Keen, D. A.; Bennett, T. D.; Wondraczek, L., Ionic liquid facilitated melting of the metal-organic framework ZIF-8. *Nat. Commun.* **2021,** *12*, 5703.
84. Kamminga, M. E.; de Wijs, G. A.; Havenith, R. W.; Blake, G. R.; Palstra, T. T., The role of connectivity on electronic properties of lead iodide perovskite-derived compounds. *Inorg. Chem.* **2017,** *56*, 8408-8414.
85. Asher, M.; Angerer, D.; Korobko, R.; Diskin-Posner, Y.; Egger, D. A.; Yaffe, O., Anharmonic Lattice Vibrations in Small-Molecule Organic Semiconductors. *Adv. Mater.* **2020,** *32*, 1908028.
86. Sharma, R.; Menahem, M.; Dai, Z.; Gao, L.; Brenner, T. M.; Yadgarov, L.; Zhang, J.; Rakita, Y.; Korobko, R.; Pinkas, I., Lattice mode symmetry analysis of the orthorhombic phase of methylammonium lead iodide using polarized Raman. *Phys. Rev. Mater.* **2020,** *4*, 051601.
87. Juhás, P.; Davis, T.; Farrow, C. L.; Billinge, S. J., PDFgetX3: a rapid and highly automatable program for processing powder diffraction data into total scattering pair distribution functions. *J. Appl. Cryst.* **2013,** *46*, 560-566.

TOC: